Constraining Between-Event Variability of Kinematic Rupture Scenarios by Empirical Ground-Motion Model: A Case Study in Central Italy

František Čejka[*1], Sara Sgobba[2], Francesca Pacor[2], Chiara Felicetta[2], Ľubica Valentová[1], and František Gallovič[1]

ABSTRACT

The region of central Italy is well known for its moderate-to-large earthquakes. Events such as 2016 M_w 6.2 Amatrice, generated in the shallow extensional tectonic regime, motivate numerical simulations to gain insights into source-related ground-motion complexities. We utilize a hybrid integral–composite kinematic rupture model by Gallovič and Brokešová (2007) to predict ground motions for other hypothetical Amatrice fault rupture scenarios (scenario events). The synthetic seismograms are computed in 1D crustal velocity models, including region-specific 1D profiles for selected stations up to 10 Hz. We create more than ten thousand rupture scenarios by varying source parameters. The resulting distributions of synthetic spectral accelerations at periods 0.2–2 s agree with the empirical nonergodic ground-motion model of Sgobba *et al.* (2021) for central Italy in terms of the mean and total variability. However, statistical mixed-effect analysis of the residuals indicates that the between-event variability of the scenarios exceeds the empirical one significantly. We quantify the role of source model parameters in the modeling and demonstrate the pivotal role of the so-called stress parameter that controls high-frequency radiation. We propose restricting the scenario variability to keep the between-event variability within the empirical value. The presented validation of the scenario variability can be generally utilized in scenario modeling for more realistic physics-based seismic hazard assessment.

KEY POINTS

- We simulate ground motions of M_w 6.2 kinematic scenarios with various source parameters for central Italy.
- Between-event scenario variability is controlled by stress parameter aggregating effects of source features.
- We propose restricting the scenarios to keep their between-event variability within the empirical value.

Supplemental Material

INTRODUCTION

Characterization of ground motions, including their uncertainty, is one of the main ingredients in seismic hazard assessment, especially for large, human-built structures such as power plants, infrastructure, or buildings in urban areas. Current approaches are based mainly on empirical ground-motion models (GMM) determined by the statistical processing of earthquake recordings. GMMs describe ground shaking as a function of source parameters, source-to-site path, and site conditions. The predictive capabilities of such models have improved in the recent years due to the increasing availability of seismic records, allowing GMMs to be regionalized by distinguishing source regions, geological domains, and/or specific soil conditions. Moreover, the use of advanced statistical techniques, such as the linear mixed-effects regression (Stafford, 2014; Bates *et al.*, 2015), made it possible to handle the variability better and to calibrate a new generation of partially or totally nonergodic GMMs (Anderson and Brune, 1999; Lin *et al.*, 2011; Rodriguez-Marek *et al.*, 2013; Kotha *et al.*, 2016; Baltay and Hanks, 2017; Abrahamson *et al.*, 2019,

1. Department of Geophysics, Faculty of Mathematics and Physics, Charles University, Czech Republic, https://orcid.org/0000-0001-6418-0029 (FC); https://orcid.org/0000-0002-9574-1105 (LV); https://orcid.org/0000-0002-9268-3923 (FG);
2. Istituto Nazionale di Geofisica e Vulcanologia, Milan, Italy, https://orcid.org/0000-0002-5669-8650 (SS); https://orcid.org/0000-0001-5745-0414 (FP); https://orcid.org/0000-0003-2852-9144 (CF)

*Corresponding author: cejka@karel.troja.mff.cuni.cz

Cite this article as Čejka, F., S. Sgobba, F. Pacor, C. Felicetta, Ľubica. Valentová, and F. Gallovič (2024). Constraining Between-Event Variability of Kinematic Rupture Scenarios by Empirical Ground-Motion Model: A Case Study in Central Italy, *Bull. Seismol. Soc. Am.* **XX**, 1–13, doi: 10.1785/0120230251

etc.). They represent a powerful tool to predict ground motions in moderate- and high-seismicity areas, where the abundance of data, especially in far-field regions, allows the models to be better constrained. Contrarily, GMMs are less resolved at near-source distances and for larger events due to their rare occurrence and the consequent paucity of recordings, even in well-instrumented regions.

This shortage of seismic records can be remedied by physics-based ground-motion simulations, which are promising to fill the observational gaps (Ameri *et al.*, 2012; Bradley *et al.*, 2017; Paolucci *et al.*, 2021). For example, the so-called hybrid simulations are employed frequently due to their efficiency in a broad frequency range (Mai and Beroza, 2003; Gallovič and Brokešová, 2007; Graves and Pitarka, 2010). They can predict ground motions for various rupture scenarios of hypothetical events in a particular region. In the case of scenario rupture modeling, the synthetic ground motions are usually assessed against the empirical GMMs. We point out that the validation of ground-motion scenario modeling is still an open issue despite being a critical prerequisite to engineering applications. For example, the Broadband Platform of the Southern California Earthquake Center (Dreger *et al.*, 2015; Goulet *et al.*, 2015) performed various validation tests against both recorded ground motions of individual events and empirical GMMs. Nevertheless, most scenario simulation validations focus only on the median prediction at the current stage. Only a few studies assess the scenario simulations by comparing their ground-motion variability with the empirical counterpart (e.g., Ameri *et al.*, 2009; Cultrera *et al.*, 2010; Song, 2016; Lin and Smerzini, 2022). Moreover, the studies are concerned only with total variability.

In the GMM community, it is common to discern two major constituents of variability: between-event (B-E) and within-event (W-E) (Strasser *et al.*, 2009; Al Atik *et al.*, 2010). Although the former corresponds to the event-dependent deviation of the ground-motion residuals averaged over all stations, the latter reflects the remaining variability over stations for a given event. We stress that the scenario modeling assessment should concern these two ingredients individually, because they provide distinct constraints. The B-E residuals are connected only to the mean source characteristics (such as mean stress drop, mean rupture velocity, etc.) that affect all stations equally. The W-E residuals thus comprehend all the individual path effects (e.g., 3D medium, hanging, or footwall), site effects, and site-specific source effects such as source directivity, asperity position, and so forth. Analysis of W-E and B-E variability from the scenario simulations poses different numerical/computational challenges. Although the W-E variability can be studied using a few rupture scenarios with complex 3D source models and 3D wave propagation (e.g., Aochi and Douglas, 2006; Dujardin *et al.*, 2018; Withers *et al.*, 2018), the B-E variability assessment requires many rupture scenarios with various mean characteristics and is rarely studied. Recently, Parker *et al.* (2023) analyzed the B-E variability from their rupture scenarios showing that the observed one is overestimated likely due to the considered slip velocities.

We point out that recognizing the two ingredients of the variability in the scenarios enables modelers to bind any unconstrained free modeling source parameters unbiasedly. In particular, the so-called stress parameter describing high-frequency radiation is known to affect ground motions dominantly (Drouet and Cotton, 2015). Yet, it is often considered constant, leading to underestimating the B-E ground-motion variability of the scenarios (r53Douglas and Aochi, 2016; Pacor *et al.*, 2016; Lee *et al.*, 2020). Alternatively, the parameter is varied in an ad hoc manner (Crempien and Archuleta, 2017) or based on a theoretical model (Drouet and Cotton, 2015), and then the synthetic B-E standard deviation is compared with the empirical one. This study explores the possibility of restricting the source model parameters set to rather ad hoc values by assessing their effects on the resulting B-E variability of the scenarios.

The target area of our study is the central Italy region (see Fig. 1a), which is well known for its relatively large seismicity and complex tectonic structure. It features mainly seismogenic structures oriented north-northwest–south-southeast driven by the extensional tectonic regime of the central Apennines. The fault segments generally dip southwest, extending 20–25 km along the strike and 10–15 km along the dip (Boncio *et al.*, 2004). Many earthquakes struck this area over the last centuries, and a large amount of data was acquired thanks to the increasing number of installed stations in the previous 40 yr that were used to derive high-quality nonergodic regional GMM (e.g., Sgobba *et al.*, 2021). The events include the 1979 M_w 5.9 Norcia, 1980 M_w 6.9 Irpinia, 1984 M_w 5.6 Gubbio, 1997 M_w 6.0 Umbria–Marche, 2009 M_w 6.1 L'Aquila, and the 2016–2017 Amatrice–Visso–Norcia sequence, with Norcia being the largest event (M_w 6.5).

The objective of the present study is to build a synthetic ground-motion dataset in a broad frequency range (0–10 Hz) of kinematic rupture scenarios using the Hybrid Integral–Composite (HIC) model for a hypothetical virtual event. As a model event, we take the 2016 M_w 6.2 Amatrice earthquake that has been extensively studied, for example, with kinematic modeling (Tinti *et al.*, 2016; Cirella *et al.*, 2018), broadband hybrid methods (Pischiutta *et al.*, 2016, 2021), or dynamic models (Gallovič *et al.*, 2019; Taufiqurrahman *et al.*, 2023). The HIC modeling approach has been validated for several central Italian events, for example, the 1980 M_w 6.9 Irpinia (Ameri *et al.*, 2011), the 2009 M_w 6.3 L'Aquila (Ameri *et al.*, 2012), and in other regions, for example, the 2011 M_w 7.1 Van (eastern Türkiye; Gallovič *et al.*, 2013), and recently the 2023 M_w 7.8 Kahramanmaraş (eastern Türkiye; Čejka *et al.*, 2023) earthquakes. Recently, Čejka *et al.* (2024) validated the HIC model against the 2016 M_w 6.2 Amatrice earthquake recordings.

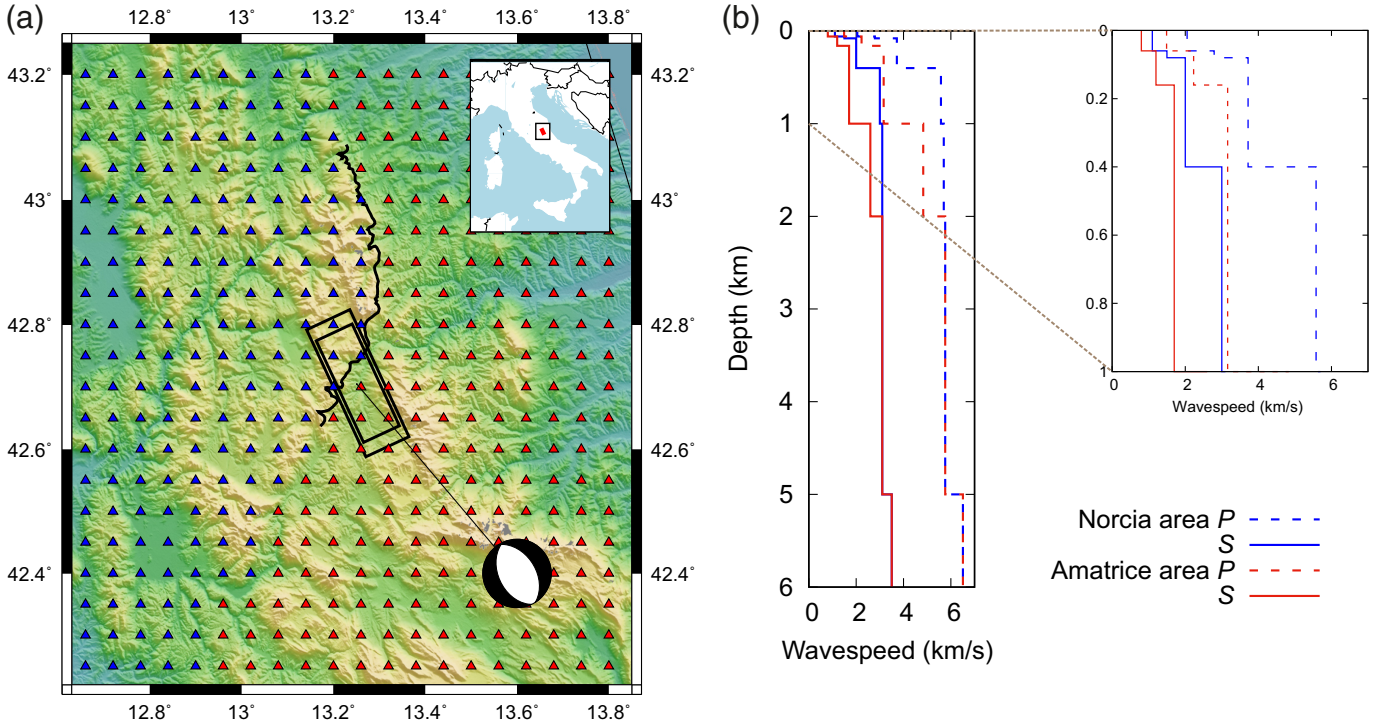

Figure 1. Study area and velocity models. (a) Epicentral area of the 2016 Amatrice earthquake with 400 virtual stations (triangles) used for ground-motion modeling with variable source scenarios. The black curves correspond to the Sibillini thrust separating different crustal regimes of the Norcia and Amatrice area. Colors distinguish velocity models used for stations in the Norcia (blue) and Amatrice areas (red). The black rectangles show the fault planes assumed in the scenario modeling, and focal mechanism plot shows the corresponding mechanism. A map of Italy with the study area depicted by a black rectangle is shown in the inset. (b) Velocity models were used to calculate Green's functions for stations in the Norcia (blue) and Amatrice (red) area, with inset zooming in the uppermost 1 km. See also Table S1 for the model definitions in numbers. The color version of this figure is available only in the electronic edition.

To build different rupture scenarios, we vary the parameters describing the HIC source model and simulate ground motions on a regular grid of receivers. We compare the synthetic response spectra at periods 0.2–2 s with the empirical regional GMM and perform mixed-effect regression on the residuals to discern the B-E and W-E variability. We explore the role of the individual source parameters contributing to the variability demonstrating the pivotal role of the stress parameter aggregating all the source parameters. The analysis also shows that the synthetic B-E variability overestimates the empirical one. Therefore, we propose to restrict the source parameters to fit the synthetic B-E variability to the empirical value, assuming that (1) the empirical B-E variability corresponds to the upper limit of the synthetic B-E variability of the scenarios, and (2) the nonergodic GMM variability constrained mainly by the abundant small- to moderate-size events is representative of the variability from less-frequent larger-magnitude events. Eventually, we discuss the relation between the stress parameters of the restricted scenario database and their estimates from empirical studies, so that the latter can be used to restrict the scenarios a priori in future studies. Our approach thus provides general guidelines for scenario generation to simulate ground motions for various seismotectonic regions worldwide where a good GMM is available.

METHODS

Source model

To generate the kinematic rupture scenarios, we employ the HIC technique in which the rupture process is represented by overlapping square sub-sources randomly distributed on the fault with fractal number-size distribution, in which the number of sub-sources decreases linearly with increasing sub-source size (see also Gallovič and Brokešová, 2007). The sub-sources are characterized by a constant stress-drop scaling composing a slip distribution with k^{-2} decay at high wavenumbers k. These sub-sources are treated differently in the high- (above f_1) and low- (up to f_2) frequency ranges, and each of these procedures results in a seismogram, which overlaps in the crossover frequency range f_1–f_2. Up to f_2, the integral of the representation theorem is calculated, assuming a rupture propagating at a constant rupture velocity. Above f_1, the composite approach is used, in which the individual sub-sources are treated as point sources with Brune's source time function. The Brune's function is described by the sub-source's seismic moment and corner frequency, assuming constant stress-drop scaling (see further for more details). In addition, we randomly vary the mechanism of the sub-sources in the composite part to weaken the radiation pattern at high frequencies. The resulting seismograms up to f_1 come purely

from the integral approach, whereas the seismograms are purely composite above f_2. As a result, the directivity of the rupture propagation is well captured at lower frequencies due to the coherent summation of the subfaults' wavefield contributions, whereas it is suppressed due to the incoherent summation of the sub-sources' wavefield contributions at high frequencies.

In the frequency crossover section (f_1–f_2), the combination of composite and integral seismograms is treated in the Fourier domain by weighted averaging of the real and imaginary parts of the two seismograms from the two approaches using $\cos^2$ and $\sin^2$ functions (see fig. 2 in Gallovič and Brokešová, 2007). The crossover frequency range f_1–f_2 is considered to cover the corner frequency of the event, which has been estimated 0.19 Hz in the Amatrice validation article (Čejka *et al.*, 2024) or empirical value of 0.35 ± 0.09 Hz from the Brune stress-drop inversion by Morasca *et al.* (2019). Following Ameri *et al.* (2012) and Čejka *et al.* (2024), who modeled the M_w 6.3 L'Aquila and M_w 6.2 Amatrice events in central Italy, respectively, we set $f_1 = 0.15$ Hz and $f_2 = 0.6$ Hz.

In the high-frequency composite part, we assume the omega-square source model, in which the height of the acceleration spectral plateau above $\hat{f}_c$ is equal to $M_0\hat{f}_c^2$, with M_0 and $\hat{f}_c$ being the total scalar seismic moment and the event corner frequency, respectively. In the HIC model, we generalize the corner frequency with $\hat{f}_c = \frac{av_r}{L}$, in which L is the rupture length, v_r is the rupture velocity, and parameter a is a tuning parameter controlling the strength of the high-frequency radiation. The height of the acceleration spectral plateau is as follows:

$$A = M_0\hat{f}_c^2 = a^2 v_r^2 \frac{M_0}{S}, \tag{1}$$

in which $S = L^2$. The proportionality constant a is considered to be related to the small-scale rupture evolution and its radiation strength. Because of this, we treat it as a free parameter in our study, although the previous studies suggested a value close to 1 (Gallovič and Brokešová, 2007; Ameri *et al.*, 2009, 2011, etc.). Parameter a can also be interpreted in terms of the so-called stress parameter $\Delta\sigma$. Considering that the latter corresponds to the stress drop of a crack model (e.g., Brune, 1970; Kaneko and Shearer, 2015; Wang and Day, 2017; Gallovič and Valentová, 2020), it reads

$$\Delta\sigma = \frac{7}{16}\left(\frac{\hat{f}_c}{kv_s}\right)^3 M_0, \tag{2}$$

in which v_s is the shear-wave velocity, and k is a parameter depending on the details of the rupture model (heterogeneity of slip, v_r, rise time, etc.). Expressing $\hat{f}_c$ from equation (2), the alternative equation describing the acceleration plateau reads

$$A = M_0\hat{f}_c^2 = k^2 v_s^2 \left(\frac{16}{7}\right)^{2/3} \Delta\sigma^{2/3} M_0^{1/3}. \tag{3}$$

Comparing equations (1) and (3) suggests that the stress parameter $\Delta\sigma$ is a combination of source parameters (rupture velocity v_r, rupture size L, and proportionality constant a) considering a fixed scalar seismic moment. Later, when analyzing our synthetic dataset, we treat $\Delta\sigma$ as a lumped (aggregate) parameter specific for each rupture scenario.

To summarize, the HIC model parameters for fixed M_0 are: (1) the fault area, (2) the nucleation point position, (3) the sub-sources layout (i.e., the slip distribution), (4) the rupture velocity, and (5) the sub-source corner frequencies (alternatively parameter a).

To generate the synthetic scenarios, we set the strike/dip/rake angles to 155°/45°/−85°, the latitude and longitude of the fault center to 42.7063° N, 13.2532° E, and the scalar seismic moment to 2.6×10^{18} N · m (Pizzi *et al.*, 2017; Gallovič *et al.*, 2019). We consider two fault dimensions, 25×12 km^2 and 20×10 km^2, representing the sizes of fault segments in central Italy. We consider 15 and 12 nucleation points distributed regularly on the fault for the larger and smaller fault, respectively (Fig. 2). We use eight slip distributions with asperity in the middle, on one or the other side, and both sides, by prescribing the position of the largest sub-sources deterministically (when the others are placed randomly). We also change the random seed to get variations of these. The resulting slip distributions are shown in Figure 2 for both the fault sizes. Note that the slip amplitudes are larger for the smaller fault since the seismic moment is fixed, although the spatial distributions are the same for the two fault sizes.

The rupture propagates from the prescribed nucleation radially at a constant speed. We vary rupture velocity v_r between 2.0 and 3.4 km/s with a step of 0.2 km/s, covering the standard range of slow to fast ruptures. The last varying parameter is a, assuming values from 0.7 to 1.9 with a step of 0.2. The parameter ranges were chosen rather ad hoc and are addressed later in the Discussion, in which they are constrained following the B-E variability of the GMM.

Green's functions and crustal velocity models

To calculate the synthetic seismograms, the HIC sub-sources are convolved with Green's functions according to the representation theorem for a regular grid of 400 virtual stations (Fig. 1a). The synthetic Green's functions are precalculated in the 1D velocity models using the Axitra code (Cotton and Coutant, 1997) at frequencies 0.05–10 Hz.

We consider a specific 1D velocity model for each of the two major geological domains divided by the Sibillini thrust, which is the main structural discontinuity in the area (Fig. 1): (1) the south-southeast unit of the Sibillini thrust, which lies on the Laga formation (Amatrice area) and (2) the carbonate unit to the north-northwest of the thrust (Norcia area). For the Amatrice area, we supplement the crustal velocity model proposed by Ameri *et al.* (2012) used in ground-motion simulations of the 2009 L'Aquila earthquake by three subsurface

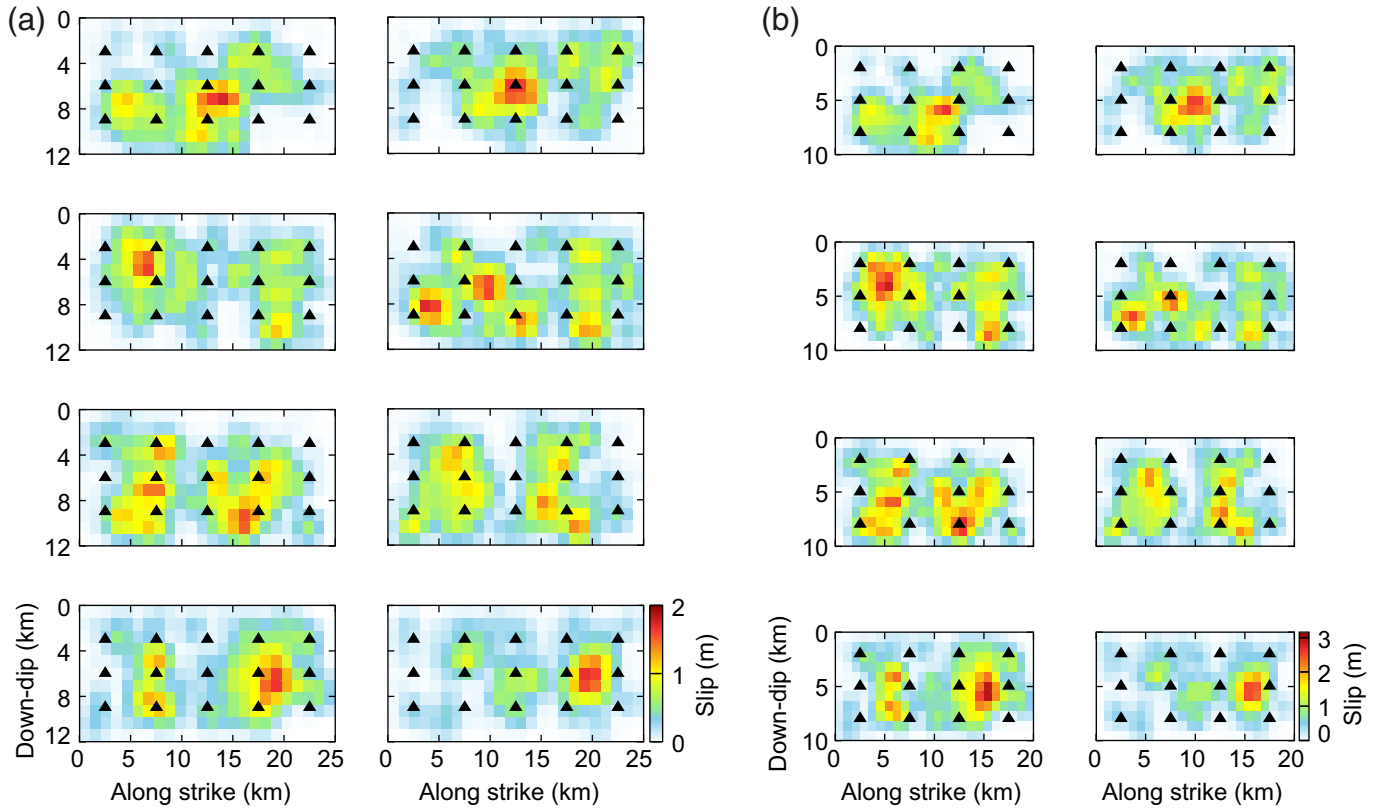

Figure 2. Eight slip distributions used in the scenario source modeling obtained by changing the distribution of sub-sources of the Hybrid Integral–Composite (HIC) model for fault sizes (a) 25×12 km^2 and (b) 20×10 km^2. The largest sub-sources are placed deterministically to simulate various positions of asperities, whereas the others are distributed randomly along the fault. The black triangles mark nucleation points from which the rupture propagates at constant speeds. Note the different color scales in the two panels. The color version of this figure is available only in the electronic edition.

low-velocity layers, as considered in kinematic and dynamic source modeling of the Amatrice earthquake by Gallovič and Valentová (2023) and Čejka *et al.* (2024), respectively. For the Norcia area, we adapt the 1D velocity model of Bianchi *et al.* (2010) to consider the observed wave propagation differences between the two main domains. The topmost kilometer in the Norcia area was obtained by resampling the V_S array profile at stations IT.CSC (Cascia) and IT.LSS (Leonessa). The two final velocity models proposed for the Amatrice and Norcia area are shown in Figure 1b and Table S1.

The anelastic attenuation is modeled by depth-dependent quality factor Q and high-frequency decay parameter κ. Following Castro *et al.* (2022), we adopt $\kappa = 0.03$ s as a mean value for all the stations.

GMM

To assess the scenarios, we compare the simulated ground motions with a fully nonergodic GMM by Sgobba *et al.* (2021), hereafter named SEA, calibrated explicitly for the region of central Italy on a dense dataset (about 30,000 waveforms) from 460 stations within 120 km from about 450 earthquakes in the magnitude range of 3.4–6.5. Unlike traditional ergodic models, the SEA is calibrated on reference rock sites (as identified by Lanzano *et al.*, 2020) and then adjusted for systematic effects related to source area, propagation path, and site response, which are specific to the target region.

In our application, the SEA median is adjusted for the location-to-location contribution related to local systematic differences in source features (stress drop, focal depth, etc.) with respect to the average overall source regions in central Italy (for more details, see Sgobba *et al.*, 2021). On the other hand, we do not introduce any site correction terms, because the predictions refer to rock conditions. Moreover, we neglect the small contribution of propagation (i.e., the path-to-path terms), because our primary purpose is to reproduce the overall empirical attenuation trend, with no specific focus on the spatial distribution of the shaking. However, the missing corrections to the median are moved to the associated total variability composed of the B-E and W-E terms (see the appendix of Sgobba *et al.*, 2021, for more details). As a result, for the present case study, the W-E variability includes the following sources of uncertainty: (1) the response of the 36 reference rock sites used for the SEA calibration, (2) the systematic path terms, and (3) the remaining aleatory variability.

The adopted GMM model is defined for the spectral accelerations (SAs). Therefore, if available, the simulations are

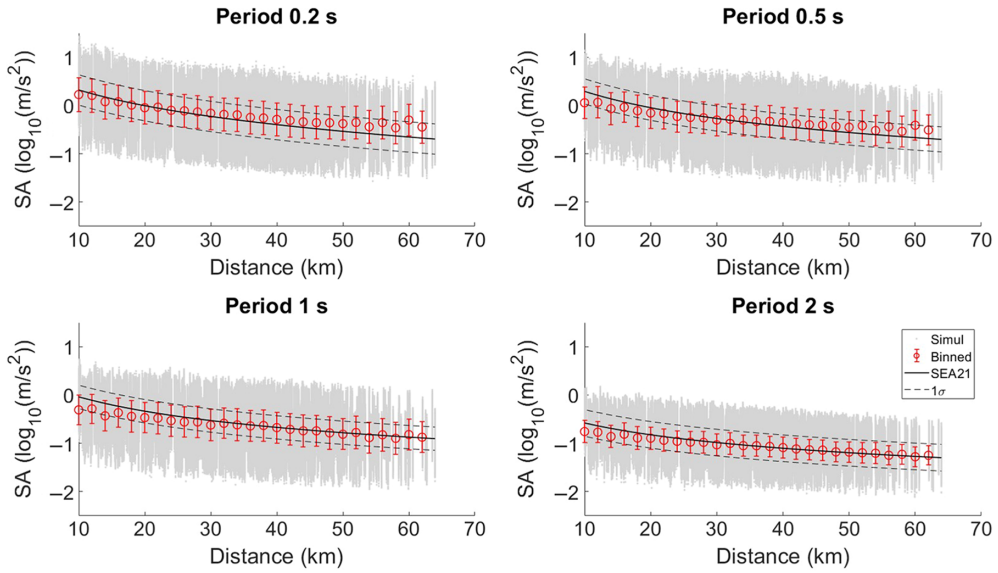

Figure 3. Spectral accelerations at four spectral ordinates at virtual receivers of Figure 1 and for all source scenarios plotted as a function of the Joyner–Boore distance by gray dots. The red circles with error bars are mean values and standard deviations over 2 km bins. The black solid and dashed lines are the ground-motion model (GMM) mean and uncertainty prediction, respectively (SEA, Sgobba *et al.*, 2021). The color version of this figure is available only in the electronic edition.

compared with GMM in terms of SA. Nevertheless, the proposed methodology can be applied to other ground-motion measures, such as Fourier amplitude spectra (Kotha *et al.*, 2022; Sgobba *et al.*, 2023).

RESULTS

Comparison with GMM and synthetic ground-motion variability

In total, we generate 12,096 source models and calculate the broadband seismograms at 400 virtual stations resulting in more than 4.8 million synthetic waveforms simulated up to the maximum frequency of 10 Hz. From them, we evaluate the response SAs for periods in the range of 0.2–2 s. Figure 3 compares SAs at four vibration periods (0.2, 0.5, 1, and 2 s) with the predictions of the SEA model for the study region. To facilitate the comparison, we supplement the figure with the mean and standard deviations of binned data. We observe a good agreement with the empirical GMM regarding median and variability at all SA ordinates. We point out that the total variability comprises the W-E (azimuthal changes) and B-E (changes due to the event characteristics) terms. We further scrutinize these two components to avoid misinterpreting the modeling performance.

To analyze the variability of the scenario simulations (Fig. 3), we use mixed-effect regression, which is standardly used in quantifying fixed and random effects of ground motions in the development of empirical GMMs (Bates *et al.*, 2015). For each spectral period, the residuals R_{ij} between decadic logarithms (log10) of geometric means of the horizontal synthetic SAs, y_{ij}, and the corresponding empirical estimates from the SEA model of Sgobba *et al.* (2021), y_{ij}^{GMM}, for event scenario i at station j, defined as $R_{ij} = y_{ij}^{\mathrm{GMM}} - y_{ij}$, can be decomposed into the following equation:

$$R_{ij} = C + \eta_i + \varepsilon_{ij}, \qquad (4)$$

in which C is the mean offset between the GMM and synthetic database; η_i are the B-E residuals representing the mean offset over all stations of the ith event scenario; and ε_{ij} are the W-E residuals corresponding to the difference of synthetic measurement at observer j from the offset of event i. These variability terms are assumed to have independent normal distributions with zero mean and standard deviations denoted τ and ϕ for the B-E and W-E variabilities, respectively. The total standard deviation is then $\sigma = \sqrt{\phi^2 + \tau^2}$. The decomposition is here performed using the Python package Statsmodel (see Data and Resources, Seabold and Perktold, 2010).

The period dependence of mean offset C, W-E deviation ϕ, B-E deviation τ, and total standard deviation σ is shown in Figure 4a (violet). Table 1 (first row) lists the values for an example period 0.2 s. The W-E variability is slightly below the empirical value of the SEA model (black) for almost all periods. This underestimation could be ascribed to the fact that the synthetic W-E variability includes only some effects (two area-specific crustal models, varying nucleation point position, radiation pattern, and directivity effects). In contrast, it lacks others, such as complex path effects due to the 3D velocity structure and topography, the uncertainty of reference rock sites, and remaining aleatory uncertainties, which are present in the real data. Note that the W-E variability is even smaller if only 1 crustal model is used (Fig. S1, available in the supplemental material to this article). We conclude that we cannot reach the empirical value of the W-E variability in our synthetic dataset by adopting Green's function modeling with 1D models.

The difference between observations and synthetics is larger for the B-E variability and increases toward the lower periods. Indeed, the scenario simulations provide about twice larger B-E standard deviations than the empirical ones for period 0.2 s ($\tau^{\mathrm{GMM}} = 0.142$ and $\tau = 0.327$, see Table 1). We attribute this significant overestimation of the synthetic B-E variability to the exaggerated scenario variability. We point out that it would remain unnoticed without the additional analysis of the

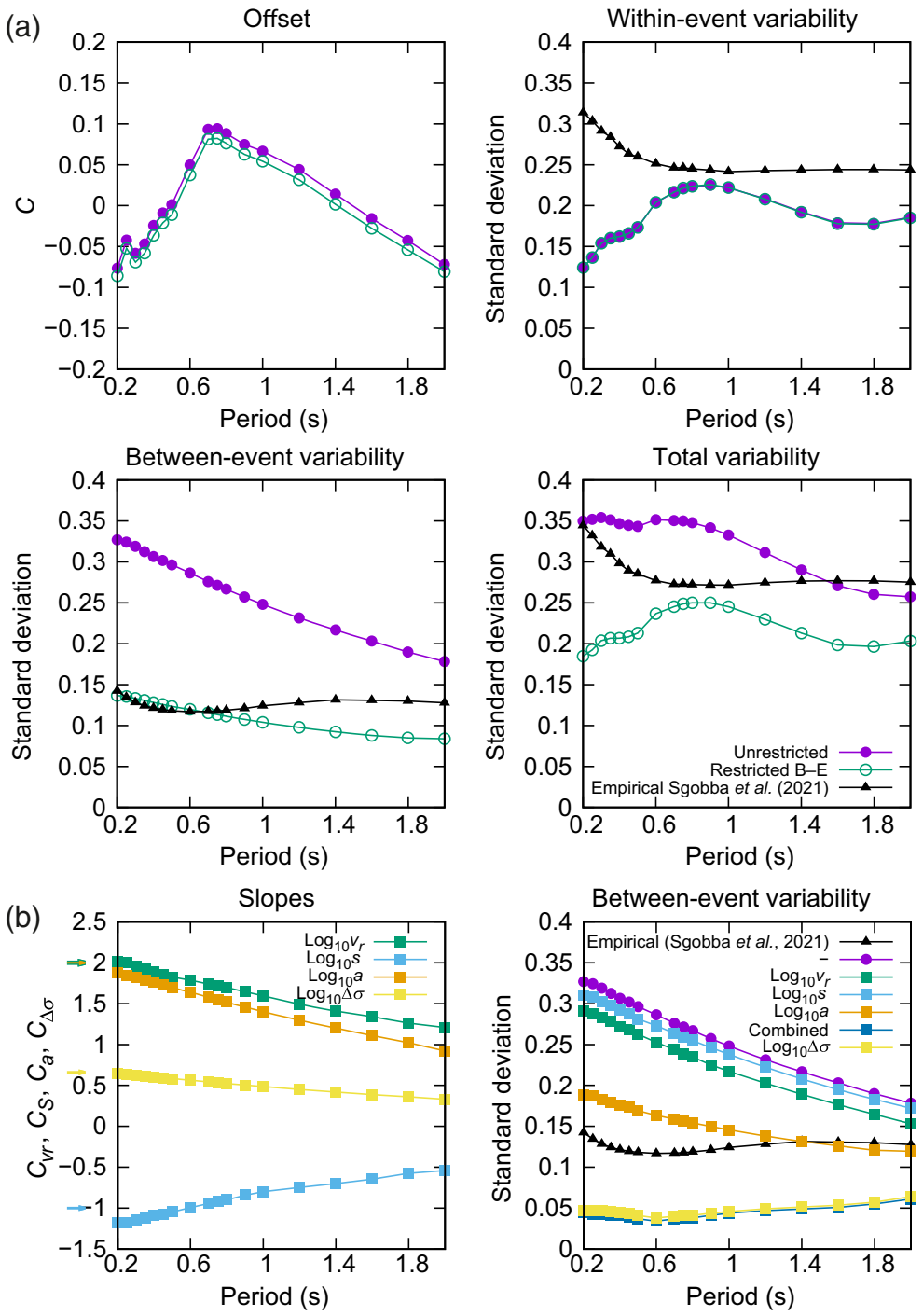

Figure 4. Results of the linear mixed-model regression of spectral acceleration residuals with respect to SEA GMM at different spectral periods. (a) Offset, within-event (W-E), between-event (B-E), and total variability standard deviation (in log10). Models with unrestricted and restricted B-E residuals (see the Constraining the Source Parameters section) are distinguished by symbols and colors. The black triangles show the empirical variability. (b) Coefficient values for the individual explanatory variables and the respective log10 standard deviation of the B-E variability (see equations 5 and 6) distinguished by colors (see legend); "combined" corresponds to the case when all the variables (except for the stress parameter) are considered together. Arrows outside the left graph are theoretical values at high frequencies, see equations (1) and (3). The purple line is the B-E variability corresponding to the mixed-model regression without any explanatory variable (equation 4), the same as in panel (a). The black line is the empirical B-E variability of the GMM by Sgobba *et al.* (2021). The color version of this figure is available only in the electronic edition.

components of the variability by the mixed-model statistics. Indeed, the total variability shown in Figure 3 and then in Figure 4a shows a relatively good agreement between the simulations and the GMM for most of the periods, because the overestimation of the synthetic B-E variability was compensated by the underestimation of the synthetic W-E variability. In the Discussion, we further scrutinize the effects of HIC source parameters on the synthetic B-E variability and propose restricting scenario parameter ranges to reduce the resulting B-E variability of the scenarios.

DISCUSSION

Role of source parameters on the ground-motion variability

To understand the contributions of the individual HIC parameters to the synthetic B-E variability, we expand the regression of equation (4), considering various explanatory terms corresponding to different varied parameters. In particular, to explain the variability of SA in Figure 4a, we derive the regression model from the logarithm of the high-frequency theoretical source spectrum of equation (1),

$$R_{ij} = C' + C_a \log a_i + C_{v_r} \log v_{r_i} + C_S \log S_i + \eta_i' + \varepsilon_{ij}, \qquad (5)$$

in which C' is the new mean offset, C_a, C_{v_r}, and C_S are regression coefficients corresponding to the respective explanatory variables indicated by the subscript; and η_i' is the new B-E residual. We perform the regressions to isolate the effects of the individual source parameters on the variability, taking one explanatory variable

TABLE 1
Parameters of the Linear Mixed-Model Regression of the Spectral Acceleration (SA) Residuals for Period T = 0.2 s with Different Explanatory Variables and Corresponding Between-Event (τ) and Within-Event (ϕ) Variabilities (See the Main Text and Equations 5 and 6)

Explanatory Variable	Offset	Log$S$	Log a	Logv_r	Log$\Delta\sigma$	τ	ϕ
–	−0.077	–	–	–	–	0.327	0.124
Log S	−9.963	−1.177	–	–	–	0.311	0.124
Log a	0.095	–	1.873	–	–	0.188	0.124
Logv_r	6.814	–	–	2.012	–	0.291	0.124
Log$a$ + Log$S$ + Logv_r	−2.901	−1.177	1.873	2.012	–	0.044	0.124
Log$\Delta\sigma$	0.995	–	–	–	0.644	0.047	0.124
Empirical GMM values (Sgobba *et al.*, 2021)	–	–	–	–	–	0.142	0.314

The first row corresponds to the regression without explanatory variables as in equation (4). Empirical values of τ^{GMM} and φ^{GMM} are specifiesd in the last row.

at a time and setting the other terms to zero. Figure 4b shows period dependence of the mixed-model regression coefficients and B-E standard deviations (values for the example period 0.2 s are listed in rows 2–4 of Table 1). Note that we do not discuss the W-E standard deviations, because the considered explanatory variables in the mixed-model regression are related exclusively to the mean source properties, and thus the W-E variability remains the same for all cases.

For short periods, the regression coefficients are generally close to their predicted theoretical values, that is, powers in equation (1), indicated by arrows on the left side of Figure 4b. The coefficients generally tend to decrease (in absolute values) with increasing periods. Theoretically, the effect of the considered parameters should attain zero for the longest periods, because the finite-source model apparently becomes a point source described solely by the (fixed) seismic moment. However, this is not the case, because our maximum analyzed period of 2 s is still shorter than the rupture duration.

The B-E variabilities estimated for each explanatory variable, corresponding to the remaining B-E variability after excluding the effect of the respective variable, are shown in Figure 4b (see also Table 1 for values for the period of 0.2 s). For example, the remaining B-E variability at period 0.2 s decreases from $\tau = 0.327$ to $\tau_S = 0.311$ after removing the dependence on the fault size. The most significant decrease of the B-E standard deviation is attained for parameter a, demonstrating that the greatest portion of our scenario variability comes from the variability in this parameter (also note that $\tau_a = 0.188$ is closer to $\tau^{GMM} = 0.142$ for period 0.2 s). The drop of the synthetic B-E variability is smaller for rupture velocity v_r than for parameter a despite the fact that they both contribute to the variability with the same regression coefficient (~2, in agreement with the second power in the theoretical model of equation 1), suggesting that parameter a has stronger control on the high-frequency radiation. The effect of the rupture velocity variations on the B-E variability is also weaker because it also translates partially in the W-E variability by altering the directivity effect. We note that the decrease of the B-E variability is controlled not only by the respective regression coefficient but also by the assumed parameter range. In this sense, the result found in this analysis cannot be generalized, because it is tied to the construction of our dataset.

Figure 4b ("Combined") and the fifth row of Table 1 show the regression results after we cleared the effects of all explanatory variables (so only the nucleation point and slip distribution are not analyzed). The B-E standard deviation decreases well below the empirical value. Because such remaining variability is relatively small, it suggests that the effect of slip distribution on B-E variability is relatively weak. We note that the nucleation position controlling the directivity effect does not influence the between-scenarios variability, because it does not make a repeatable contribution to the ground motion. Conversely, it controls the spatial variability of the shaking within the same scenario event and is thus attributable to the W-E variability component.

As discussed in the Source model section, the source parameters that control the high-frequency spectrum can be lumped into one stress parameter $\Delta\sigma$ (equation 3). For each scenario, we determine the amplitude of the high-frequency acceleration source spectrum plateau by summing contributions from the HIC model sub-sources and calculate $\Delta\sigma$ by equation (3), assuming k = 0.37 (Brune, 1970). The histogram of the stress parameters for all the scenario events is shown in Figure 5, resembling a lognormal distribution.

To analyze the effect of $\Delta\sigma$ on the residuals, we assume another form of the regression equation for the residuals,

$$R_{ij} = C'' + C_{\Delta\sigma} \log \Delta\sigma + \eta_i'' + \varepsilon_{ij}, \tag{6}$$

in which C'' is the mean offset value, and $C_{\Delta\sigma}$ is the regression coefficient for $\Delta\sigma$ as the explanatory variable. The results are shown in Figure 4b (in yellow) and listed in Table 1 for the 0.2 s period. The value of the coefficient $C_{\Delta\sigma}$ is 0.64, which is very close to the theoretically derived value ⅔ in equation (3). As expected, the low value of the remaining B-E standard

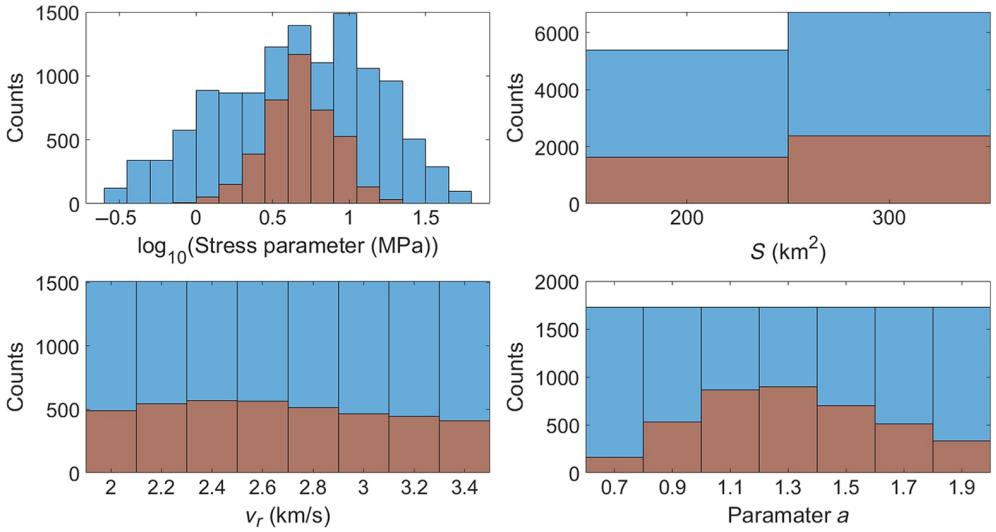

Figure 5. Histograms of source model parameters of the scenario database. The blue bars correspond to the unrestricted (full) database, and the brown bars are for scenarios restricted to have the B-E residuals in agreement with the adopted GMM. The color version of this figure is available only in the electronic edition.

deviation (like the case of the combined regression) confirms the validity of equation (3), suggesting that the scenario variability is controlled dominantly by this aggregated parameter. Note also that the mutually canceling effect of the source parameters lumped in the stress parameter makes the B-E standard deviation stable over all periods.

Constraining the source parameters

As we have shown, the B-E variability of our scenario simulations exceeds its empirical counterpart. This calls for restricting the scenario variability by limiting their source parameters for further applications. We propose reducing the number of scenarios by constraining the synthetic B-E standard deviation τ to be close to the empirical value τ^{GMM} of Sgobba *et al.* (2021). Indeed, this GMM is a regional model describing the source contributions of the seismogenic structures with normal-fault mechanisms in central Italy.

We prescribe the probability density function (PDF) of the synthetic B-E residuals at the lowest considered period of 0.2 s to follow the empirical form, namely normal PDF with zero mean and standard deviation to be equal to the empirical value of the adopted GMM at 0.2 s. We use the rejection method, in which we randomly pick scenarios and accept or reject them stochastically based on their B-E residual. This way, the B-E residuals of the resulting restricted database have PDF that agrees with the empirical one at 0.2 s; at higher periods, the B-E standard deviations are closer to or below the empirical values (Fig. 4a). In the restricted database, we choose to have about one-third of the scenario events (4000 scenarios with potential duplicate entries).

We explore the properties of the source parameters of the scenarios in the restricted database. The stress parameter has a narrower lognormal distribution with a mean of 4.3 MPa and log10 variability of 0.23 (see Fig. 5). The distributions of fault dimension S, rupture velocity v_r, and parameter a are shown in Figure 5. We see that S and v_r retain their distributions from the unrestricted dataset, whereas parameter a attains a bell shape instead of uniform distribution. This is due to the exclusion of many "extreme" scenarios also associated with too high- or too low-stress parameters.

Concerning the ground-motion variability, the restricted scenario events database does not affect the offset and the W-E standard deviation (Fig. 4a, green). The former is because we assumed a zero mean for the prescribed PDF of the B-E residuals; if needed, prescribing a nonzero mean can be used to adjust the offset with respect to the empirical GMM. The combination of the B-E and W-E components also makes the total variability of the restricted dataset slightly smaller than the empirical one (Fig. 4a). This is, however, preferable, considering the unmodeled features such as complex 3D path and variability among reference rock sites. In addition, there is no epistemic uncertainty in our synthetic dataset (e.g., in magnitude) that would increase the variabilities as in empirical estimates, because we know all our modeling parameters perfectly (Crempien and Archuleta, 2017; Valentová *et al.*, 2021). Indeed, Figure S3 shows that the B-E variability of the restricted database reaches the empirical value if we add random perturbation to each scenario's M_{w} (with ±0.1 standard deviation), representing the error in M_{w} estimation from real data.

Because the only constraint in the restricted database is placed on the synthetic B-E residuals and not the source model parameters, we examine the possible correlations between the parameters in the restricted database. For example, comparing the expressions for the spectral acceleration plateau from equations (1) and (3), we obtain the following equation:

$$\Delta\sigma = \frac{7}{16}\left(\frac{a}{k}\frac{v_r}{v_s}\right)^3 \frac{M_0}{S^{3/2}}, \tag{7}$$

in which we see a possible correlation between the stress parameter $\Delta\sigma$ and, for example, rupture velocity v_r. Although we see such a correlation in the unrestricted database, the stress parameter is independent of the rupture velocity in the restricted

database (see Fig. S2a). This can be explained by the anticorrelation between v_r and a, which was not originally present in the scenario database, as suggested also by equation (7), see Figure S2b. We point out that the anticorrelation is an outcome of the scenario restriction. Nevertheless, adopting such a relationship from physical considerations (rupture dynamics) would be preferable.

Relation of the B-E variability to the stress-drop variability

There is a long-lasting debate about whether the B-E variability is connected to the variability of stress drop or stress parameter (Atkinson and Beresnev, 1997; Causse and Song, 2015; Gallovič and Valentová, 2020). Moreover, the relation between the stress drop and stress parameter is ambiguous. In empirical studies, the stress drop is usually estimated using corner frequencies under the assumption of the Brune (omega-square) source model (equation 2) (Abercrombie, 2021). On the other hand, the stress parameter is related to the high-frequency ground motions (equation 3). The two empirical estimates are discrepant both in mean and variability, so they are suggested to be understood as two distinct, unrelated quantities (Atkinson and Beresnev, 1997).

There are two main reasons for this discrepancy. First, the epistemic error in the corner frequency estimation is amplified by the third power in the relation between the corner frequency and the stress drop (equation 2), increasing the variability of the inferred Brune stress drop. Second and more substantial is the validity of the Brune model itself. For complex models, the source spectra deviate from the simple Brune spectra, and the corner frequency thus estimated is not directly related to stress conditions on the fault. Indeed, this issue has been recognized in real-event analyses (Archuleta and Ji, 2016; Denolle and Shearer, 2016; Liu *et al.*, 2023) and dynamic source modeling (Gallovič and Valentová, 2020).

On the contrary, the HIC source model employed in this study is based on the Brune source spectrum (although strictly speaking, the Brune model is considered for the individual subsources). Therefore, the stress drop estimated from the corner frequency is directly related to the stress parameter controlling the high-frequency spectral radiation. For this reason, we found that the ratio between standard deviations of the high-frequency B-E ground-motion variability τ^{GMM} (0.142 in log10) and the calculated Brune stress parameter $\Delta\sigma$ of the restricted database (0.23 in log10) is close to the coefficient $C_{\Delta\sigma}$ from the residual regression analysis (equation 6) and the theoretically derived relation with power ⅔ (equation 3),

$$\tau \sim C_{\Delta\sigma}\mathrm{std}(\log\Delta\sigma) = 0.64\mathrm{std}(\log\Delta\sigma) \approx 2/3\mathrm{std}(\log\Delta\sigma). \quad (8)$$

An alternative theoretical relation between PGA variability and the stress parameter with a similar scaling coefficient of 5/6 was derived by Causse *et al.* (2008) and validated by Drouet and Cotton (2015). Our resulting value of 0.64 permits a larger variability of the stress parameter to fit the B-E variability than in Causse *et al.* (2008). Nevertheless, it depends on the methodology and thus can deviate from other theoretical predictions.

The relation between the standard deviation of the stress parameter and the B-E residuals (equation 8) can be thus utilized when generating scenarios using models based on the Brune spectrum. Let us emphasize that adopting empirical stress-drop standard deviation to determine that of the stress parameter would lead to too large scenario variability. Indeed, in the standard empirical estimates from corner frequencies of apparent moment rate functions of real earthquakes, the Brune stress-drop variability is inferred as 0.5 in log10 (i.e., 1.1 in ln; e.g., Baltay *et al.*, 2011; Cotton *et al.*, 2013; Causse and Song, 2015; Oth *et al.*, 2017; Bindi, Picozzi, *et al.*, 2018; Bindi, Spallarossa, *et al.*, 2018; Morasca *et al.*, 2022, and references therein). Adopting this value for the stress parameter variability, that is, corresponding roughly to our unrestricted database, would result in the scenario B-E variability of 0.3 in log10 (0.7 in ln), much higher than the empirical estimate. Contrarily, the standard deviation of the stress parameter of our restricted database is 0.23 in log10, as if it was constrained by the empirical B-E value ($\tau^{\mathrm{GMM}} = 0.142$ and equation 7). Although this analysis was made a posteriori on our dataset, for future applications the stress-drop/parameter variability of the synthetic scenarios can be constrained a priori from the empirical B-E variability using equation (8). Because $\Delta\sigma$ aggregates effects of all other source parameters, one can also randomly sample parameters v_r, a, and S independently from their uniform distributions and limit the scenarios a priori (i.e., before performing the simulations), so that the resulting distribution of the stress parameter follows its target distribution with a prescribed standard deviation of $\Delta\sigma$.

Let us also note that the empirical B-E variability might be biased by epistemic errors, such as uncertainty in the M_w estimation, as suggested by dynamic simulations (Valentová *et al.*, 2021) and data analysis of large, repeating earthquakes (Yagoda-Biran *et al.*, 2015). Considering this overestimation in the empirical values, the stress parameter variability for the scenario simulations would be even smaller than the value derived from the B-E one using equation (8). We acknowledge that our approach of constraining the scenario variability represents an upper limit.

CONCLUSIONS

We have employed a kinematic finite-fault model to build a database of ~12,000 M_w 6.2 earthquake scenarios with varied source-related parameters. The total variability of the simulated scenarios agrees with the empirical one. The mixed-model analysis reveals that when the synthetic W-E variability is underestimated, the B-E variability (i.e., purely the variability due to changes in the source scenarios) exceeds the empirical

values. The former is acceptable, considering the simplification of many path and site complexities in the modeling. However, the overestimation of the synthetic B-E variability related to the changes in source scenarios suggests too large variability in the mean source parameters.

To overcome this issue, we restricted the scenario database by randomly resampling the scenarios to conform their B-E residuals with the prescribed (empirical) distribution. We showed that the standard deviation of the stress parameter (aggregating all source modeling parameters in our models) attains ∼⅔ of the empirical B-E standard deviation of the adopted GMM, in agreement with theoretical considerations for our kinematic model. This relation can be used for future applications to restrict a priori the stress parameter variability of the scenarios (instead of adopting the likely overestimated variability from empirical source spectrum studies). In addition, the stress parameter variability can be considered even smaller for a single seismogenic source, because the empirical B-E standard deviation is affected by epistemic errors.

DATA AND RESOURCES

The Python package Statsmodel is available at www.statsmodels.org (last accessed September 2023). The supplemental material contains Table S1 with the 1D crustal velocity model of (a) Norcia area and (b) Amatrice area. Figure S1 shows the decrease of the within-event (W-E) variability if one 1D crustal model is considered. Figure S2 demonstrates the relations between the stress parameter and rupture velocity and between the parameter a and rupture velocity in the original and restricted scenario databases. Figure S3 documents the increase of the between-event (B-E) variability of the restricted database if we add random perturbation to each scenario's M_w (with ±0.1 standard deviation), representing the error in M_w estimation from real data. The study is based solely on synthetic calculations.

DECLARATION OF COMPETING INTERESTS

The authors acknowledge that there are no conflicts of interest recorded.

ACKNOWLEDGMENTS

The authors thank C. Mascandola for providing the velocity models of the Amatrice and Norcia areas. The authors acknowledge financial support from the Czech Science Foundation (Project Number 23-06345S) and Charles University Project Number SVV 115–09/260581 as well as the Istituto Nazionale di Geofisica e Vulcanologia (INGV) "Ricerca Libera" 2021 project HSE-GMM (S. Sgobba) "A hybrid simulation-empirical approach to model variability of ground motion in near-source region". This research is also partially supported by INGV in the frame of the project SECURE (Regional-Scale Earthquake Ground Motion PrediCtions ThroUgh Pyhsics-based and EmpiRical ApproachEs: A Case study central Italy) within Pianeta Dinamico (Working Earth)—Geosciences for the Understanding of the Dynamics of the Earth and the Consequent Natural Risks (CUP code D53J19000170001) funded by the Italian Ministry of University and Research (MIUR). The authors thank Fabrice Cotton and an anonymous reviewer for their constructive suggestions that helped improve the article.

REFERENCES

Abercrombie, R. E. (2021). Resolution and uncertainties in estimates of earthquake stress drop and energy release, *Phil. Trans. Roy. Soc. Lond. A.* **379,** 20200131, doi: 10.1098/rsta.2020.0131.

Abrahamson, N. A., N. M. Kuehn, M. Walling, and N. Landwehr (2019). Probabilistic seismic hazard analysis in California using nonergodic ground-motion models, *Bull. Seismol. Soc. Am.* **109,** no. 4, 1235–1249.

Al Atik, L., N. Abrahamson, J. J. Bommer, F. Scherbaum, F. Cotton, and N. Kuehn (2010). The variability of ground-motion prediction models and its components, *Seismol. Res. Lett.* **81,** no. 5, 794–801.

Ameri, G., A. Emolo, F. Pacor, and F. Gallovič (2011). Ground-motion simulations for the 1980 M 6.9 Irpinia earthquake (southern Italy) and scenario events, *Bull. Seismol. Soc. Am.* **101,** no. 3, 1136–1151.

Ameri, G., F. Gallovič, and F. Pacor (2012). Complexity of the M_w 6.3 2009 L'Aquila (central Italy) earthquake: 2. Broadband strong-motion modeling, *J. Geophys. Res.* **117,** no. B4, doi: 10.1029/2011JB008729.

Ameri, G., F. Gallovič, F. Pacor, and A. Emolo (2009). Uncertainties in strong ground-motion prediction with finite-fault synthetic seismograms: An application to the 1984 M 5.7 Gubbio, Central Italy, earthquake, *Bull. Seismol. Soc. Am.* **99,** no. 2A, 647–663, doi: 10.1785/0120080240.

Anderson, J. G., and J. N. Brune (1999). Probabilistic seismic hazard analysis without the ergodic assumption, *Seismol. Res. Lett.* **70,** no. 1, 19–28.

Aochi, H., and J. Douglas (2006). Testing the validity of simulated strong ground motion from the dynamic rupture of a finite fault, by using empirical equations, *Bull. Earthq. Eng.* **4,** 211–229, doi: 10.1007/s10518-006-0001-3.

Archuleta, R. J., and C. Ji (2016). Moment rate scaling for earthquakes $3.3 \le M \le 5.3$ with implications for stress drop, *Geophys. Res. Lett.* **43,** no. 23, 12,004–12,011.

Atkinson, G. M., and I. Beresnev (1997). Don't call it stress drop, *Seismol. Res. Lett.* **68,** 3–4.

Baltay, A., and T. Hanks (2017). Uncertainty, variability, and earthquake physics in ground-motion prediction equations, *Bull. Seismol. Soc. Am.* **107,** doi: 10.1785/0120160164.

Baltay, A., S. Ide, G. Prieto, and G. Beroza (2011). Variability in earthquake stress drop and apparent stress, *Geophys. Res. Lett.* **38,** L06303, doi: 10.1029/2011GL046698.

Bates, D., B. Mächler, B. Bolker, and S. Walker (2015). Fitting linear mixed-effects models using lme4, *J. Stat. Software* **67,** no. 1, 1–48.

Bianchi, I., C. Chiarabba, and N. P. Agostinetti (2010). Control of the 2009 L'Aquila earthquake, central Italy, by a high-velocity structure: A receiver function study, *J. Geophys. Res.* **115,** no. B12, doi: 10.1029/2009JB007087.

Bindi, D., M. Picozzi, D. Spallarossa, F. Cotton, and R. Kotha (2018). Impact of magnitude selection on aleatory variability associated with ground-motion prediction equations: Part II–Analysis of the between-event distribution in central Italy, *Bull. Seismol. Soc. Am.* **109,** no. 1, 251–262.

Bindi, D., D. Spallarossa, M. Picozzi, D. Scafidi, and F. Cotton (2018). Impact of magnitude selection on aleatory variability associated with ground-motion prediction equations: Part I–Local, energy, and moment magnitude calibration and stress-drop variability in central Italy, *Bull. Seismol. Soc. Am.* **108,** no. 3A, 1427–1442, doi: 10.1785/0120170356.

Boncio, P., G. Lavecchia, and B. Pace (2004). Defining a model of 3D seismogenic sources for seismic hazard assessment applications: The case of central Apennines (Italy), *J. Seismol.* **8,** 407–425, doi: 10.1023/B:JOSE.0000038449.78801.05.

Bradley, B., D. Pettinga, J. Baker, and J. Fraser (2017). Guidance on the utilization of earthquake-induced ground motion simulations in engineering practice, *Earthq. Spectra* **33**, doi: 10.1193/120216eqs219ep.

Brune, J. N. (1970). Tectonic stress and the spectra of seismic shear waves from earthquakes, *J. Geophys. Res.* **75,** no. 26, 4997–5009, doi: 10.1029/JB075i026p04997.

Castro, R., L. Colavitti, C. Vidales-Basurto, F. Pacor, S. Sgobba, and G. Lanzano (2022). Near-source attenuation and spatial variability of the spectral decay parameter kappa in central Italy, *Seismol. Res. Lett.* **93,** 1–12.

Causse, M., and S. G. Song (2015). Are stress drop and rupture velocity of earthquakes independent? Insight from observed ground motion variability, *Geophys. Res. Lett.* **42,** 7383–7389, doi: 10.1002/2015GL064793.

Causse, M., F. Cotton, C. Cornou, and P.-Y. Bard (2008). Calibrating median and uncertainty estimates for a practical use of empirical Green's functions technique, *Bull. Seismol. Soc. Am.* **98,** 344–353.

Čejka, F., Ľ. Valentová Krišková, S. Sgobba, F. Pacor, C. Felicetta, and F. Gallovič (2024). Ground motion modeling of the 2016 M_w 6.2 Amatrice (Italy) earthquake by a broadband hybrid kinematic approach, including empirical site effects, *Seismol. Res. Lett.* (under revision).

Čejka, F., J. Zahradník, F. Turhan, E. Sokos, and F. Gallovič (2023). Long-period directivity pulses of strong ground motion during the 2023 M_w 7.8 Kahramanmaraş earthquake, *Commun. Earth Environ.* **4,** 413, doi: 10.1038/s43247-023-01076-x.

Cirella, A., G. Pezzo, and A. Piatanesi (2018). Rupture kinematics and structural-rheological control of the 2016 M_w 6.1 Amatrice (central Italy) earthquake from joint inversion of seismic and geodetic data, *Geophys. Res. Lett.* **45,** 12,302–12,311, doi: 10.1029/2018GL080894.

Cotton, F., and O. Coutant (1997). Dynamic stress variations due to shear faults in a plane-layered medium, *Geophys. J. Int.* **128,** no. 3, 676–688, doi: 10.1111/j.1365-246X.1997.tb05328.x.

Cotton, F., R. Archuleta, and M. Causse (2013). What is sigma of the stress drop? *Seismol. Res. Lett.* **84,** no. 1, 42–48, doi: 10.1785/0220120087.

Crempien, J. G. F., and R. J. Archuleta (2017). Within-event and between-events ground motion variability from earthquake rupture scenarios, *Pure Appl. Geophys.* **174,** 3451–3465, doi: 10.1007/s00024-017-1615-x.

Cultrera, G., A. Cirella, E. Spagnuolo, A. Herrero, E. Tinti, and F. Pacor (2010). Variability of kinematic source parameters and its implication on the choice of the design scenario, *Bull. Seismol. Soc. Am.* **100,** no. 3, 941–953, doi: 10.1785/0120090044.

Denolle, M. A., and P. M. Shearer (2016). New perspectives on self-similarity for shallow thrust earthquakes, *J. Geophys. Res.* **121,** no. 9, 6533–6565.

Douglas, J., and H. Aochi (2016). Assessing components of ground-motion variability from simulations for the Marmara Sea region (Turkey), *Bull. Seismol. Soc. Am.* **106,** 300–306.

Dreger, D. S., G. C. Beroza, S. M. Day, C. A. Goulet, T. H. Jordan, P. A. Spudich, and J. P. Stewart (2015). Validation of the SCEC broadband platform V14. 3 simulation methods using pseudo spectral acceleration data, *Seismol. Res. Lett.* **86,** no. 1, 39–47.

Drouet, S., and F. Cotton (2015). Regional stochastic GMPEs in low-seismicity areas: Scaling and aleatory variability analysis—Application to the French Alps, *Bull. Seismol. Soc. Am.* **105,** 1883–1902.

Dujardin, A., M. Causse, C. Berge-Thierry, and F. Hollender (2018). Radiation patterns control the near-source ground-motion saturation effect, *Bull. Seismol. Soc. Am.* **108,** no. 6, 3398–3412.

Gallovič, F., and J. Brokešová (2007). Hybrid k-squared source model for strong ground motion simulations: Introduction, *Phys. Earth Planet. In.* **160,** 34–50, doi: 10.1016/j.pepi.2006.09.002.

Gallovič, F., and Ľ. Valentová (2020). Earthquake stress drops from dynamic rupture simulations constrained by observed ground motions, *Geophys. Res. Lett.* **47,** e2019GL085880, doi: 10.1029/2019GL085880.

Gallovič, F., and Ľ. Valentová (2023). Broadband strong ground motion modeling using planar dynamic rupture with fractal parameters, *J. Geophys. Res.* **128,** e2023JB026506, doi: 10.1029/2023JB026506.

Gallovič, F., G. Ameri, J. Zahradník, J. Janský, V. Plicka, E. Sokos, A. Askan, and M. Pakzad (2013). Fault process and broadband ground-motion simulations of the 23 October 2011 Van (eastern Turkey) earthquake, *Bull. Seismol. Soc. Am.* **103,** 3164–3178.

Gallovič, F., Ľ. Valentová, J.-P. Ampuero, and A.-A. Gabriel (2019). Bayesian dynamic finite-fault inversion: 2. Application to the 2016 M_w 6.2 Amatrice, Italy, earthquake, *J. Geophys. Res.* **124,** 6970–6988.

Goulet, C. A., N. A. Abrahamson, P. G. Somerville, and K. E. Wooddell (2015). The SCEC broadband platform validation exercise: Methodology for code validation in the context of seismic-hazard analyses, *Seismol. Res. Lett.* **86,** no. 1, 17–26.

Graves, R., and A. Pitarka (2010). Broadband ground-motion simulation using a hybrid approach, *Bull. Seismol. Soc. Am.* **100,** 2095–2123.

Kaneko, Y., and P. M. Shearer (2015). Variability of seismic source spectra, estimated stress drop, and radiated energy, derived from cohesive-zone models of symmetrical and asymmetrical circular and elliptical ruptures, *J. Geophys. Res.* **120,** 1053–1079, doi: 10.1002/2014JB011642.

Kotha, S. R., D. Bindi, and F. Cotton (2016). Partially non-ergodic region specific GMPE for Europe and Middle-East, *Bull. Earthq. Eng.* **14,** 1245–1263.

Kotha, S. R., D. Bindi, and F. Cotton (2022). A regionally adaptable ground-motion model for Fourier amplitude spectra of shallow crustal earthquakes in Europe, *Bull. Earthq. Eng.* **20,** 711–740.

Lanzano, G., Ch Felicetta, F. Pacor, D. Spallarossa, and P. Traversa (2020). Methodology to identify the reference rock sites in regions of medium-to-high seismicity: An application in central Italy, *Geophys. J. Int.* **222,** 2053–2067, doi: 10.1093/gji/ggaa261.

Lee, R. L., A. Brendon, P. J. Bradley, R. W. Stafford, A. Graves, and M. Rodriguez (2020). Hybrid broadband ground motion simulation validation of small magnitude earthquakes in Canterbury, New Zealand, *Earthq. Spectra* **36,** 673–699, doi: 10.1177/8755293019891718.

Lin, J., and C. Smerzini (2022). Variability of physics-based simulated ground motions in Thessaloniki urban area and its implications for seismic risk assessment, *Front. Earth Sci.* **10,** 951781, doi: 10.3389/feart.2022.951781.

Lin, P.-S., B. Chiou, N. Abrahamson, M. Walling, C.-T. Lee, and C.-T. Cheng (2011). Repeatable source, site, and path effects on the

standard deviation for empirical ground-motion prediction models, *Bull. Seismol. Soc. Am.* **101,** 2281–2295.

Liu, M., Y. Huang, and J. Ritsema (2023). Characterizing multisubevent earthquakes using the Brune source model, *Bull. Seismol. Soc. Am.* **113,** no. 2, 577–591, doi: 10.1785/0120220192.

Mai, P., and G. C. Beroza (2003). A hybrid method for calculating near-source, broadband seismograms: Application to strong motion prediction, *Phys. Earth Planet. In.* **137,** 183–199.

Morasca, P., D. Bindi, K. Mayeda, J. Roman-Nieves, J. Barno, W. R. Walter, and D. Spallarossa (2022). Source scaling comparison and validation in central Italy: Data intensive direct S-waves versus the sparse data coda envelope methodology, *Geophys. J. Int.* **231,** no. 3, 1573–1590, doi: 10.1093/gji/ggac268.

Morasca, P., W. R. Walter, K. Mayeda, and M. Massa (2019). Evaluation of earthquake stress parameters and its scaling during the 2016-2017 Amatrice-Norcia-Visso sequence—Part I, *Geophys. J. Int.* **218,** no. 1, 446–455, doi: 10.1093/gji/ggz165.

Oth, A., H. Miyake, and D. Bindi (2017). On the relation of earthquake stress drop and ground motion variability, *J. Geophys. Res.* **122,** 5474–5492, doi: 10.1002/2017JB014026.

Pacor, F., D. Spallarossa, A. Oth, L. Luzi, R. Puglia, L. Cantore, A. Mercuri, M. D'Amico, and D. Bindi (2016). Spectral models for ground motion prediction in the L'Aquila region (central Italy): Evidence for stress-drop dependence on magnitude and depth, *Geophys. J. Int.* **204,** no. 2, 697–718, doi: 10.1093/gji/ggv448.

Paolucci, R., C. Smerzini, and M. Vanini (2021). BB-SPEEDset: A validated dataset of broadband near-source earthquake ground motions from 3D physics-based numerical simulations, *Bull. Seismol. Soc. Am.* **111,** no. 5, 2527–2545.

Parker, G. A., M. P. Moschetti, and E. M. Thompson (2023). Ground-motion variability from kinematic rupture models and the implications for nonergodic probabilistic seismic hazard analysis, *Seismol. Res. Lett* doi: 10.1785/0220220380.

Pischiutta, M., A. Akinci, L. Malagnini, and A. Herrero (2016). Characteristics of the strong ground motion from the 24th August 2016 Amatrice earthquake, *Ann. Geophys.* **59,** doi: 10.4401/AG-7219.

Pischiutta, M., A. Akinci, E. Tinti, and A. Herrero (2021). Broad-band ground-motion simulation of 2016 Amatrice earthquake, central Italy, *Geophys. J. Int.* **224,** no. 3, 1753–1779, doi: 10.1093/gji/ggaa412.

Pizzi, A., A. Di Domenica, F. Gallovič, L. Luzi, and R. Puglia (2017). Fault segmentation as constraint to the occurrence of the main shocks of the 2016 central Italy seismic sequence, *Tectonics* **36,** 2370–2387, doi: 10.1002/2017TC004652.

Rodriguez-Marek, A., F. Cotton, N. A. Abrahamson, S. Akkar, L. Al Atik, B. Edwards, G. A. Montalva, and H. M. Dawood (2013). A model for single-station standard deviation using data from various tectonic regions, *Bull. Seismol. Soc. Am.* **103,** no. 6, 3149–3163, doi: 10.1785/0120130030.

Seabold, S., and J. Perktold (2010). Statsmodels: Econometric and statistical modeling with python, *Proc. of the 9th Python in Science Conference*, Austin, Texas, 28 June–3 July 2010, doi: 10.25080/Majora-92bf1922-011.

Sgobba, S., G. Lanzano, L. Colavitti, P. Morasca, M. C. D'Amico, and D. Spallarosa (2023). Physics-based parametrization of a FAS nonergodic ground motion model for central Italy, *Bull. Earthq. Eng.* **21,** 4111–4137.

Sgobba, S, G Lanzano, and F Pacor (2021). Empirical nonergodic shaking scenarios based on spatial correlation models: An application to central Italy, *Earthq. Eng. Struct Dynam.* **50,** 60–80, doi: 10.1002/eqe.3362.

Song, G. S. (2016). Developing a generalized pseudo-dynamic source model of M_w 6.5–7.0 to simulate strong ground motions, *Geophys. J. Int.* **204,** no. 2, 1254–1265, doi: 10.1093/gji/ggv521.

Stafford, P. J. (2014). Crossed and nested mixed-effects approaches for enhanced model development and removal of the ergodic assumption in empirical ground-motion models, *Bull. Seismol. Soc. Am.* **104,** no. 2, 702–719, doi: 10.1785/0120130145.

Strasser, F. O., N. A. Abrahamson, and J. J. Bommer (2009). Sigma: Issues, insights, and challenges, *Seismol. Res. Lett.* **80,** no. 1, 40–56.

Taufiqurrahman, T., A.-A. Gabriel, T. Ulrich, Ľ. Valentová, and F. Gallovič (2023). Broadband dynamic rupture modeling with fractal fault roughness, frictional heterogeneity, viscoelasticity and topography: The 2016 M_w 6.2 Amatrice, Italy earthquake, *Geophys. Res. Lett.* **49,** e2022GL098872, doi: 10.1029/2022GL098872.

Tinti, E., L. Scognamiglio, A. Michelini, and M. Cocco (2016). Slip heterogeneity and directivity of the M_L 6.0, 2016, Amatrice earthquake estimated with rapid finite-fault inversion, *Geophys. Res. Lett.* **43,** 10,745–10,752, doi: 10.1002/2016GL071263.

Valentová, Ľ., F. Gallovič, and S. Hok (2021). Near-source ground motions and their variability derived from dynamic rupture simulations constrained by NGA-West2 GMPEs, *Bull. Seismol. Soc. Am.* **111,** no. 5, 2559–2573, doi: 10.1785/0120210073.

Wang, Y., and S. M. Day (2017). Seismic source spectral properties of crack-like and pulse-like modes of dynamic rupture, *J. Geophys. Res.* **122,** 6657–6684, doi: 10.1002/2017JB014454.

Withers, K. B., K. B. Olsen, Z. Shi, and S. M. Day (2018). Validation of deterministic broadband ground motion and variability from dynamic rupture simulations of buried thrust earthquakes, *Bull. Seismol. Soc. Am.* **109,** no. 1, 212–228, doi: 10.1785/0120180005.

Yagoda-Biran, G., J. G. Anderson, H. Miyake, and K. Koketsu (2015). Between-event variance for large repeating earthquakes, *Bull. Seismol. Soc. Am.* **105,** no. 4, 2023–2040, doi: 10.1785/0120140196.

Manuscript received 11 October 2023
Published online 14 March 2024